


# Nuclear Equation of State for Arbitrary Proton Fraction and Temperature Based on Chiral Effective Field Theory and a Gaussian Process Emulator

J. Keller<sup>1,2,\*</sup>, K. Hebeler<sup>1,2,3,†</sup> and A. Schwenk<sup>1,2,3,‡</sup>

<sup>1</sup>*Technische Universität Darmstadt, Department of Physics, 64289 Darmstadt, Germany*

<sup>2</sup>*ExtreMe Matter Institute EMMI, GSI Helmholtzzentrum für Schwerionenforschung GmbH, 64291 Darmstadt, Germany*

<sup>3</sup>*Max-Planck-Institut für Kernphysik, Saupfercheckweg 1, 69117 Heidelberg, Germany*

 (Received 5 May 2022; revised 9 December 2022; accepted 12 January 2023; published 17 February 2023)

We calculate the equation of state of asymmetric nuclear matter at finite temperature based on chiral effective field theory interactions to next-to-next-to-next-to-leading order. Our results assess the theoretical uncertainties from the many-body calculation and the chiral expansion. Using a Gaussian process emulator for the free energy, we derive the thermodynamic properties of matter through consistent derivatives and use the Gaussian process to access arbitrary proton fraction and temperature. This enables a first nonparametric calculation of the equation of state in beta equilibrium, and of the speed of sound and the symmetry energy at finite temperature. Moreover, our results show that the thermal part of the pressure decreases with increasing densities.

DOI: [10.1103/PhysRevLett.130.072701](https://doi.org/10.1103/PhysRevLett.130.072701)

**Introduction.**—The nuclear equation of state (EOS) plays a central role for the physics of nuclei and dense matter in neutron stars, supernovae, and mergers [1–5]. While first principle calculations for a wide range of densities, electron fractions, and temperatures are desirable, practical calculations are limited by uncertainties of the interactions in dense matter and the included degrees of freedom. At nuclear densities  $n \sim n_0$  (with saturation density  $n_0 = 0.16 \text{ fm}^{-3}$ ), neutrons and protons are the relevant degrees of freedom and chiral effective field theory (EFT) provides a systematic expansion of the strong interactions among nucleons [6–8]. This has enabled first principles studies of the EOS using various many-body approaches and including theoretical uncertainty estimates [9–26], where most calculations have focused on pure neutron matter or symmetric nuclear matter. In particular, the combination of chiral EFT results for neutron matter and neutron star observations has led to important constraints for the EOS in astrophysics and for the properties of neutron stars [27–38].

In this Letter, we calculate the EOS for arbitrary proton fractions and temperatures based on chiral EFT interactions to high order. We then construct a Gaussian process emulator of the free energy that enables nonparametric evaluations of the EOS and thermodynamic derivatives for

arbitrary nuclear conditions, including beta equilibrium, to provide direct results for neutron star matter based on chiral EFT.

**Methods.**—Our asymmetric nuclear matter calculations are based on many-body perturbation theory (MBPT) around a self-consistent Hartree-Fock (HF) state. The framework for evaluating MBPT diagrams using Monte Carlo integration is based on our previous works [22,26]. We start from the grand-canonical potential,

$$\Omega(\mu_n, \mu_p, T) = -T \ln \text{Tr}(e^{-(H - \mu_n n_n V - \mu_p n_p V)/T}), \quad (1)$$

with temperature  $T$ , volume  $V$ , and  $\mu_{\tau=n,p}$  are the neutron and proton chemical potentials with corresponding densities  $n_\tau$ . The Hamiltonian  $H = H_0 + V_{\text{NN}} + V_{\text{3N}}$  contains a kinetic term together with nucleon-nucleon (NN) and three-nucleon (3N) interactions constructed from chiral EFT up to next-to-next-to-next-to-leading order (N<sup>3</sup>LO). The MBPT series at finite  $T$  is organized following Refs. [39,40] with the same choice of reference system as in Ref. [26]. We include all contributions from NN and 3N interactions up to second order, and at third order all interaction vertices that are NN or 3N with one line closing on itself (corresponding to the normal-ordered two-body approximation). This has been shown to be a very good approximation at  $T = 0$  [22] and for neutron matter at finite  $T$  [26]. For our main results, we employ the NN interactions of Entem, Machleidt, and Nosyk (EMN) with cutoff  $\Lambda = 450 \text{ MeV}$  [41] and 3N interactions fit to nuclear saturation at N<sup>2</sup>LO ( $c_D = 2.25, c_E = 0.07$ ) and N<sup>3</sup>LO ( $c_D = 0, c_E = -1.32$ ) [22]. We include NN partial waves up to total angular momenta  $J_{12} \leq 12$ , and 3N channels up

Published by the American Physical Society under the terms of the [Creative Commons Attribution 4.0 International license](https://creativecommons.org/licenses/by/4.0/). Further distribution of this work must maintain attribution to the author(s) and the published article's title, journal citation, and DOI.

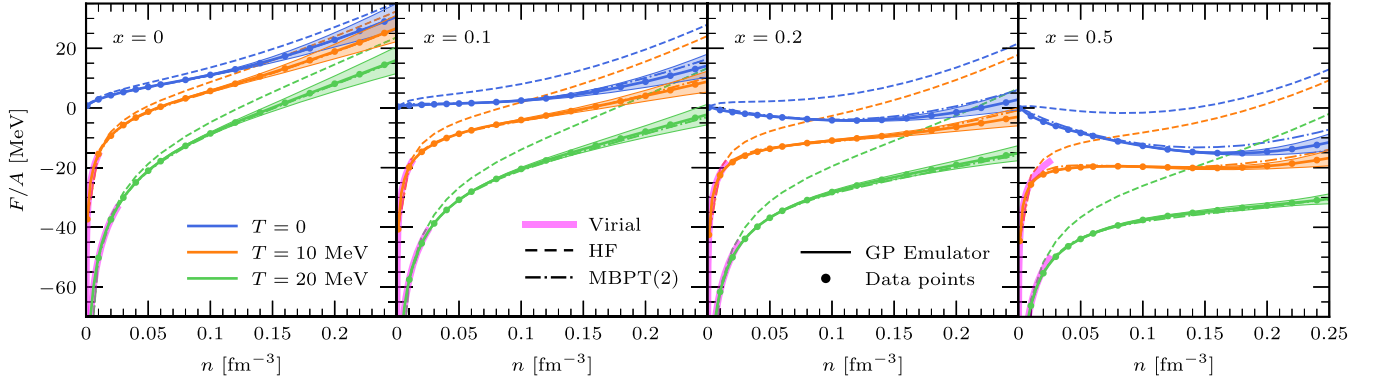


FIG. 1. Free energy per particle  $F/A$  at  $N^3\text{LO}$  ( $\Lambda = 450$  MeV) for different proton fractions  $x = 0, 0.1, 0.2,$  and  $0.5$  (panels from left to right) and for temperatures  $T = 0, 10,$  and  $20$  MeV (blue, orange, and green) as a function of density  $n$ . Our MBPT results are given by the dots, while the constructed GP emulator is shown with solid lines. The bands display theoretical EFT uncertainty estimates according to Eq. (3). To show the MBPT convergence, results at the HF level (dashed) and at second order (dot-dashed) are given as well. At low densities  $n \leq 0.025 \text{ fm}^{-3}$ , we also compare to the virial EOS [47,48] (for  $T = 20$  MeV this corresponds to a neutron fugacity  $z_n \leq 0.45, 0.39, 0.34, 0.18$  for  $x = 0, 0.1, 0.2, 0.5$ ).

to  $J_{\text{tot}} \leq 9/2$  and  $J_{12} \leq 6$  [42]. These truncations lead to uncertainties that are small compared to the EFT uncertainties for the considered densities.

The free energy density  $F/V$  is determined by

$$\frac{F}{V}(n, x, T) = \frac{\Omega}{V}(\mu_n, \mu_p, T) + \mu_n n_n(\mu_n, \mu_p, T) + \mu_p n_p(\mu_n, \mu_p, T), \quad (2)$$

where the densities are given by  $n_\tau = -\partial_{\mu_\tau} \Omega/V$ , the total density is  $n = n_n + n_p$ , and  $x = n_p/n$  is the proton fraction. To obtain the free energy, Eq. (2), as a function of density, we invert the relation between densities and chemical potentials by generalizing the method from Ref. [43] to multiple chemical potentials. In doing so, we formally expand the chemical potentials around a reference system with the same density and proton fraction as the interacting system. This re-expansion is necessary to obtain a perturbation series that is consistent with the zero-temperature formalism, and effectively deals with the anomalous diagrams at finite  $T$  [26,43,44].

As the evaluation of MBPT diagrams involves the computation of high-dimensional phase-space integrals, the computation of the thermodynamic potential for a large number of densities, temperatures and proton fractions is a complex task. Hence, for the evaluation of the free energy per particle and its derivatives, we construct an emulator for  $F(n, x, T)/A$  using three dimensional Gaussian process (GP) regression [45]. Gaussian processes allow us to interpolate the EOS in a way that does not spoil thermodynamic consistency (e.g., second-order derivatives commute) and to handle residual noise from the Monte Carlo integration. We use the Python library of Ref. [46] and employ the squared exponential kernel [45] with an overall

scale and three length scales as hyperparameters that are determined by maximizing the likelihood. In constructing the GP, we assume that each diagram has  $\Delta E_d = 5$  keV noise from the Monte Carlo integration and the total noise of every EOS point is calculated as  $\sqrt{\sum_d \Delta E_d^2}$  where the sum is over all diagrams. The resulting total noise is much smaller than interaction uncertainties due to the chiral EFT expansion and is not visible in the plots. We treat the Fermi gas (FG) contribution analytically and emulate the interaction energy per particle  $F_{\text{int}}/A = F/A - F_{\text{FG}}/A$ . The GP emulator can be performed in any set of variables. However, replacing  $n$  by the Fermi momentum  $k_F = (3\pi^2 n/2)^{1/3}$  was found to simplify the evaluation of derivatives. Moreover, all input variables are normalized to  $[0, 1]$  to prevent numerical artifacts in the GP.

*Free energy and GP emulation.*—In Fig. 1 we present results for  $F/A$  as a function of density for different proton fractions and temperatures. We evaluate the MBPT diagrams on the nonuniform grid with values  $n = 0.001, 0.01, 0.02, \dots, 0.05, 0.06, 0.08, \dots, 0.32 \text{ fm}^{-3}$ ,  $x = 0, 0.1, \dots, 0.7$ , and  $T = 0, 5, 10, 15, 20, 30$  MeV. The EOS points are marked with dots in Fig. 1, while the results obtained from the GP emulator are shown as solid lines. An excellent agreement is evident.

At low densities and finite  $T$ , we compare our results to the model-independent virial EOS [47,48] in Fig. 1. Since we consider homogeneous matter, we do not include the contributions from alpha particles in the virial EOS (i.e., we compare against Ref. [48] for  $n_\alpha = 0$ ) For  $n \leq 0.025 \text{ fm}^{-3}$  and low fugacities, we find excellent agreement with our results. For higher densities, the inclusion of higher virial coefficients and effects due to the effective nucleon mass play an important role.

TABLE I. MBPT convergence of the free energy per particle  $F/A$  in MeV at N<sup>2</sup>LO and N<sup>3</sup>LO for different proton fractions  $x$ , temperatures  $T$  in MeV, and densities  $n$  in fm<sup>-3</sup>. The EFT uncertainties determined by Eq. (3) are given in parentheses for the third-order MBPT results.

$T$	$n$	MBPT	$x = 0.3$		$x = 0.5$	
			N <sup>2</sup> LO	N <sup>3</sup> LO	N <sup>2</sup> LO	N <sup>3</sup> LO
0	0.1	HF	-0.6	0.8	-3.1	-1.6
0	0.1	2	-8.7	-8.4	-12.4	-12.1
0	0.1	3	-8.9(5)	-8.8(2)	-12.9(4)	-12.7(1)
0	0.16	HF	3.1	4.6	-0.1	1.4
0	0.16	2	-8.5	-8.3	-13.4	-13.1
0	0.16	3	-10.1(11)	-9.9(5)	-15.5(9)	-15.1(4)
0	0.2	HF	7.9	9.1	4.5	5.5
0	0.2	2	-6.1	-6.1	-11.6	-11.5
0	0.2	3	-8.6(27)	-8.7(13)	-14.6(24)	-14.7(10)
20	0.1	HF	-23.4	-23.3	-26.3	-26.1
20	0.1	2	-33.6	-34.1	-37.7	-38.1
20	0.1	3	-33.3(9)	-33.4(5)	-37.6(8)	-37.5(4)
20	0.16	HF	-13.5	-13.7	-16.7	-17.1
20	0.16	2	-28.9	-29.9	-34.1	-35.1
20	0.16	3	-29.8(11)	-29.0(6)	-35.5(7)	-34.3(7)
20	0.2	HF	-6.4	-7.2	-9.7	-10.8
20	0.2	2	-25.7	-27.3	-31.5	-33.1
20	0.2	3	-27.7(17)	-26.7(9)	-34.2(11)	-32.7(9)

For estimates of the theoretical uncertainties for an observable  $X$  due to the truncated chiral expansion we use the prescription of Ref. [49],

$$\Delta X^{(j)} = Q \cdot \max(|X^{(j)} - X^{(j-1)}|, \Delta X^{(j-1)}), \quad (3)$$

where  $X^{(j)}$  is the observable calculated at N<sup>j</sup>LO and the expansion parameter is  $Q = p/\Lambda_b$ , where we take  $\Lambda_b = 500$  MeV for the EFT breakdown scale and  $p$  is a typical momentum for the observable of interest. We take  $p$  to be the root-mean-square momentum of the Fermi gas

$p^2 = \langle k^2 \rangle = 3T[\sum_{\tau} m_{\tau}^{5/2} F_{3/2}(\mu_{\tau}/T)]/[\sum_{\tau} m_{\tau}^{3/2} F_{1/2}(\mu_{\tau}/T)]$ , where the chemical potentials  $\mu_{\tau}$  are determined from the density  $n_{\tau} = 2^{-1/2}(m_{\tau}T/\pi)^{3/2}F_{1/2}(\mu_{\tau}/T)$  and  $F_n(x) = \Gamma(n+1)^{-1} \int_0^{\infty} dt t^n [1 + \exp(t-x)]^{-1}$  are Fermi integrals. The resulting EFT uncertainty bands at N<sup>3</sup>LO are shown for the third-order MBPT results in Fig. 1. In addition, we show the first-order (HF) and second-order MBPT(2) results to assess the MBPT convergence of the expansion. Table I gives numerical values at fiducial  $n, x, T$  to document the MBPT and chiral convergence. Overall, we find a systematic MBPT convergence. For the first-order liquid-gas phase transition in symmetric nuclear matter, our results give the preliminary ranges for the critical temperature, density, and pressure,  $T_c = 15.9$ – $16.3$  MeV,  $n_c = 0.07$ – $0.11$  fm<sup>-3</sup>, and  $P_c = 0.30$ – $0.40$  MeV fm<sup>-3</sup>, where the ranges are obtained by considering the N<sup>3</sup>LO interaction at MBPT(3) and MBPT(2). A full analysis will be the topic of future work.

*Pressure and thermal effects.*—The pressure  $P = n^2 \partial_n (F/A)|_{x,T} = P_{\text{FG}} + n^2 \partial_n (F_{\text{int}}/A)|_{x,T}$  is shown in Fig. 2 for different proton fractions and temperatures, where the derivative of the interaction energy  $F_{\text{int}}/A$  is calculated using the GP emulator. As expected, the pressure decreases with increasing proton fraction, and for very neutron-rich conditions depends only weakly on the temperature for  $n \gtrsim n_0$ . Interestingly, for symmetric matter we find that the pressure decreases with increasing temperature for  $n \gtrsim 0.2$  fm<sup>-3</sup>. This negative thermal expansion has also been observed in Ref. [16] for low-momentum interactions. For neutron-rich matter, this behavior is seen in Fig. 2 starting at higher densities.

To investigate this further, we show the thermal pressure  $P_{\text{th}} = P(T) - P(T=0)$  in Fig. 3 for neutron matter and symmetric matter for  $T = 20$  MeV. We find that the thermal pressure starts to decrease at  $n \approx 0.15$  fm<sup>-3</sup> and becomes negative around  $n \approx 0.2$  fm<sup>-3</sup>. For neutron matter this finding is consistent with Ref. [26] and can be understood in terms of a neutron effective mass  $m_n^*$  that increases at higher density due to repulsive 3N contributions [23,26] [ $P_{\text{th}} \leq 0$  requires  $\partial m_n^*/\partial n_n \geq 0$ , see Eqs. (39)

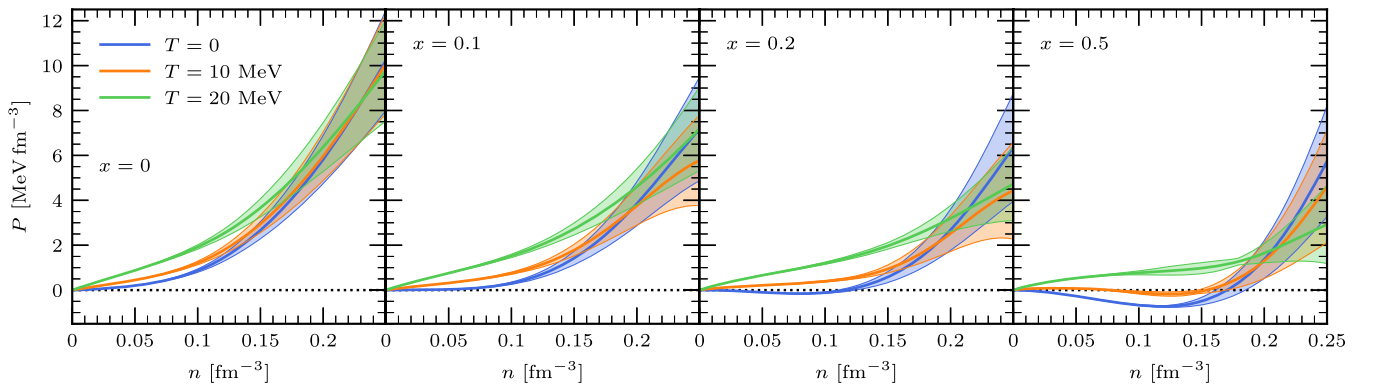


FIG. 2. Same as Fig. 1 but for the pressure  $P$  at N<sup>3</sup>LO ( $\Lambda = 450$  MeV) from the GP emulator and with EFT uncertainties.

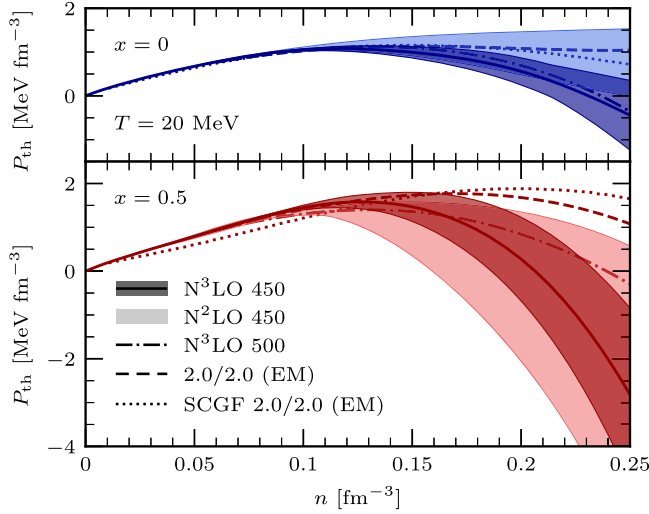


FIG. 3. Thermal pressure  $P_{\text{th}}$  for neutron matter (blue) and symmetric matter (red) for  $T = 20$  MeV as a function of density. In addition to the  $N^3\text{LO}$  results with  $\Lambda = 450$  MeV (solid lines) we also show  $\Lambda = 500$  MeV (dot-dashed lines) as well as for the 2.0/2.0 (EM) interaction [10] (dashed lines). For the latter, we compare against the SCGF results from Ref. [23] (dotted lines). The darker EFT uncertainty bands are  $N^3\text{LO}$ , while the lighter ones are for  $N^2\text{LO}$ .

and (41) in Ref. [26]]. Figure 3 shows that a decreasing thermal pressure at higher densities is found at different orders ( $N^2\text{LO}$  and  $N^3\text{LO}$ ), different cutoffs ( $\Lambda = 450$  and  $500$  MeV), as well as for the 2.0/2.0 (EM) interaction [10], while the size of the decrease has large theoretical uncertainties. For the 2.0/2.0 (EM) interaction, we can also compare our MBPT against self-consistent Green's function (SCGF) results [23] and find good agreement (with the small differences likely due to the  $T = 0$  extrapolation and the normal-ordering approximation in Ref. [23]). Note that the cutoff dependence of the negative thermal expansion might indicate that the maximal density accessible is limited based on the employed interactions.

*Matter in beta equilibrium.*—Using the GP, we can access arbitrary proton fractions and derive other quantities through thermodynamically consistent derivatives. We first use the GP to calculate the proton fraction  $x$  of neutron star matter in beta equilibrium as a function of density for different temperatures. For a given density and temperature,  $x$  is determined by the condition  $m_n + \mu_n = m_p + \mu_p + m_e + \mu_e$ , where the neutron and proton chemical potentials are given by  $\mu_\tau = F/A + n\partial_n(F/A) + (\delta_{\tau,p} - x)\partial_x(F/A)$ . The electron chemical potential is determined from the density of an ultrarelativistic Fermi gas,  $n_e = 2/\pi^2 T^3 F_2(\mu_e/T)$  with the Fermi integral  $F_2$  through charge neutrality  $n_p = n_e$ . Our results using the GP emulator are shown in the upper panel of Fig. 4. We find very narrow EFT uncertainty bands in this case, using again Eq. (3) with  $Q = Q(n, x = x_{\beta\text{-eq}}^{N^3\text{LO}}(n, T), T)$ . At small

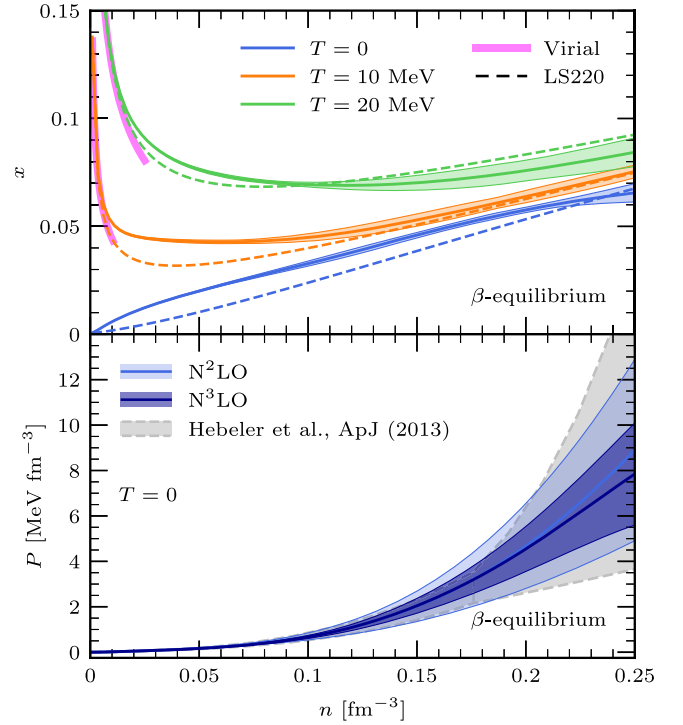


FIG. 4. Upper panel: Proton fraction  $x$  in beta equilibrium at  $N^3\text{LO}$  for different  $T$  as a function of density. For comparison, we show the virial EOS and the LS220 EOS [50]. Lower panel: Pressure  $P$  in beta equilibrium for  $T = 0$  at  $N^2\text{LO}$  and  $N^3\text{LO}$ . We compare against the EOS band from Hebel *et al.* [27] based on chiral EFT interactions up to  $1.1n_0$  and a general piecewise polytrope extension to higher densities.

densities and finite  $T$ , the proton fraction is dominated by the kinetic part and follows the virial EOS. At higher densities, the density dependence of  $x$  is weaker, with proton fractions of 4%–8% for the temperatures considered. Overall, we find a reasonable agreement with the Lattimer and Swesty EOS LS220 [50] but our chiral EFT results exhibit a weaker density dependence.

The GP thus also enables a first nonparametric calculation of the neutron star EOS. In the lower panel of Fig. 4 we show the pressure of matter in beta equilibrium  $P(n, x_{\beta\text{-eq}}, T = 0)$  at  $N^2\text{LO}$  and  $N^3\text{LO}$  with EFT uncertainty estimates. The  $N^3\text{LO}$  band is systematically smaller and overlaps with the  $N^2\text{LO}$  band over the full density range. Moreover, both bands behave naturally towards higher densities and hence show no indication for a breakdown of the chiral expansion up to  $n \lesssim 0.25 \text{ fm}^{-3}$ . For comparison, we also show the EOS band from Hebel *et al.* [27] based on chiral EFT interactions up to  $1.1n_0$  and a general piecewise polytrope extension to higher densities constrained by causality and the observation of two-solar-mass neutron stars. This EOS band results mainly from variations of the chiral 3N forces, so that the comparison is not direct. Nevertheless, the overlap with the nonparametric  $N^2\text{LO}$  and  $N^3\text{LO}$  bands is remarkable. Up to  $n_0$ , the  $N^3\text{LO}$  band prefers high pressures



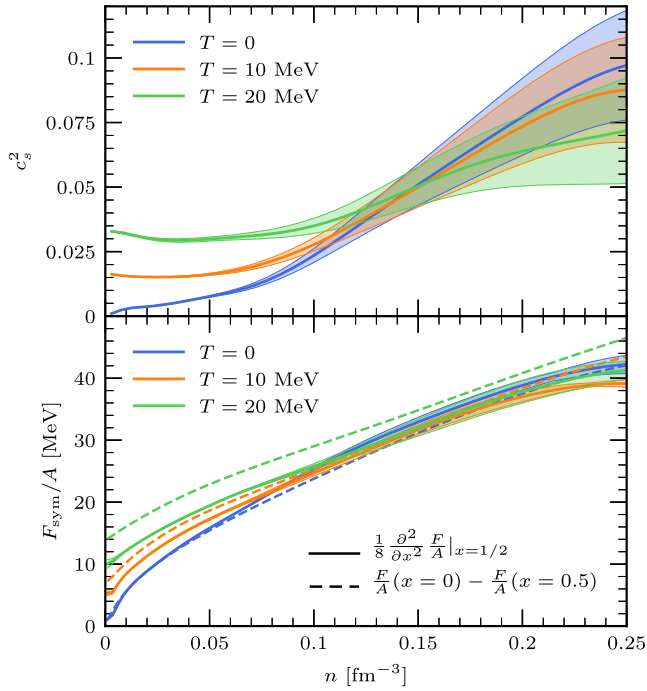


FIG. 5. Speed of sound squared  $c_s^2$  for neutron matter (upper panel) and symmetry free energy per particle  $F_{\text{sym}}/A$  (lower panel) at  $N^3\text{LO}$  for different  $T$  as a function of density. We show results based on different definitions for  $F_{\text{sym}}/A$  (second derivative around symmetric matter and difference between neutron and symmetric matter).

in the Hebeler *et al.* band [27] and at higher  $n$ , it provides important new constraints.

*Speed of sound and symmetry energy.*—Next, we study the speed of sound  $c_s^2 = \partial P / \partial \epsilon|_{S,x} = (n/P + \epsilon) \partial P / \partial n|_{S,x}$  with the internal energy density  $\epsilon = n(E/A + m_n)$ . The derivative at constant entropy  $S$  and constant proton fraction  $x$  is performed numerically based on  $P[n, x, T(n, x, S)]$ . Our results using the GP emulator are shown for neutron matter in the upper panel of Fig. 5. Given that  $c_s^2$  is a second derivative, the EFT uncertainties are larger in this case. At  $T = 0$ ,  $c_s^2$  increases monotonously while the increase is weaker at finite  $T$ . As for the pressure,  $c_s^2$  decreases at higher densities with increasing  $T$ .

As another GP application, we show the symmetry free energy per particle  $F_{\text{sym}}/A$  as a function of density for different  $T$  in the lower panel of Fig. 5. We compare two common definitions: the second derivative around symmetric matter and the difference between neutron matter and symmetric matter, where the difference probes the size of contributions beyond a quadratic  $x$  dependence. Since the numerical uncertainties are enhanced in second derivatives due to residual noise from the Monte Carlo integration, we calculate  $\partial^2(F/A)/\partial x^2|_{x=1/2}$  by fitting a GP to each MBPT diagram individually. The difference definition is more sensitive to thermal effects due to the nonquadratic contributions contained in the kinetic part.

For the second-derivative definition, we find that  $F_{\text{sym}}/A$  is narrowly predicted at  $N^3\text{LO}$  at a fixed saturation density  $n_0$ , with  $F_{\text{sym}}(n_0)/A \approx 30$  MeV at  $T = 0$ , while the uncertainty increases if one allows this reference density to vary [51]. Moreover, the  $T$  dependence of the symmetry energy is mild at  $n_0$ , with larger increases at lower and higher  $n$ .

*Conclusions and outlook.*—We presented first microscopic calculations of the EOS at arbitrary proton fractions and finite temperature based on chiral NN and 3N interactions to  $N^3\text{LO}$ , including uncertainty estimates from the many-body calculation and the chiral expansion. For this an emulator of the interaction free energy per particle was constructed using Gaussian processes. We demonstrated that this enables an efficient and accurate evaluation of the EOS and thermodynamic derivatives for arbitrary values of  $n$ ,  $x$ , and  $T$ , where we considered the ranges  $n \leq 0.25 \text{ fm}^{-3}$ ,  $x \leq 0.5$ , and  $T \leq 20$  MeV. The EFT uncertainties dominate over the MBPT uncertainties for these nuclear densities.

We studied in detail the dependence of the free energy and the pressure on proton fraction and temperature, and found that the pressure at higher densities decreases with increasing temperature, thus exhibiting a negative thermal expansion. The GP emulator allowed us to calculate the EOS in beta equilibrium directly without parametrizations between neutron and symmetric matter. The resulting  $N^3\text{LO}$  neutron star EOS exhibited a systematic chiral EFT behavior over the full range ( $n \leq 0.25 \text{ fm}^{-3}$ ) and significantly improved the uncertainties over previous EOS bands, preferring larger values for the pressure. Moreover, we presented first microscopic results for the speed of sound and the symmetry energy at finite temperature. Our framework and results test commonly applied approximation for the proton fraction and temperature dependence of the EOS and open the door to nonparametric EOS input for astrophysical simulations of supernovae and mergers.

We thank P. Arhuis for providing benchmark expressions for  $T = 0$  MBPT diagrams. This work was supported by the Deutsche Forschungsgemeinschaft (DFG, German Research Foundation)—Project-ID 279384907—SFB 1245 and by the State of Hesse within the Research Cluster ELEMENTS (Project ID 500/10.006).

\*j.keller@theorie.ikp.physik.tu-darmstadt.de

†kai.hebeler@physik.tu-darmstadt.de

‡schwenk@physik.tu-darmstadt.de

- [1] J. M. Lattimer and Y. Lim, *Astrophys. J.* **771**, 51 (2013).
- [2] K. Hebeler, J. D. Holt, J. Menéndez, and A. Schwenk, *Annu. Rev. Nucl. Part. Sci.* **65**, 457 (2015).
- [3] J. E. Lynn, I. Tews, S. Gandolfi, and A. Lovato, *Annu. Rev. Nucl. Part. Sci.* **69**, 279 (2019).
- [4] C. Drischler, J. W. Holt, and C. Wellenhofer, *Annu. Rev. Nucl. Part. Sci.* **71**, 403 (2021).
- [5] J. M. Lattimer, *Annu. Rev. Nucl. Part. Sci.* **71**, 433 (2021).

- [6] E. Epelbaum, H.-W. Hammer, and Ulf-G. Meißner, *Rev. Mod. Phys.* **81**, 1773 (2009).
- [7] R. Machleidt and D. R. Entem, *Phys. Rep.* **503**, 1 (2011).
- [8] H.-W. Hammer, S. König, and U. van Kolck, *Rev. Mod. Phys.* **92**, 025004 (2020).
- [9] K. Hebeler and A. Schwenk, *Phys. Rev. C* **82**, 014314 (2010).
- [10] K. Hebeler, S. K. Bogner, R. J. Furnstahl, A. Nogga, and A. Schwenk, *Phys. Rev. C* **83**, 031301(R) (2011).
- [11] I. Tews, T. Krüger, K. Hebeler, and A. Schwenk, *Phys. Rev. Lett.* **110**, 032504 (2013).
- [12] J. W. Holt, N. Kaiser, and W. Weise, *Prog. Part. Nucl. Phys.* **73**, 35 (2013).
- [13] A. Carbone, A. Polls, and A. Rios, *Phys. Rev. C* **88**, 044302 (2013).
- [14] G. Hagen, T. Papenbrock, A. Ekström, K. A. Wendt, G. Baardsen, S. Gandolfi, M. Hjorth-Jensen, and C. J. Horowitz, *Phys. Rev. C* **89**, 014319 (2014).
- [15] L. Coraggio, J. W. Holt, N. Itaco, R. Machleidt, L. E. Marcucci, and F. Sammarruca, *Phys. Rev. C* **89**, 044321 (2014).
- [16] C. Wellenhofer, J. W. Holt, N. Kaiser, and W. Weise, *Phys. Rev. C* **89**, 064009 (2014).
- [17] C. Wellenhofer, J. W. Holt, and N. Kaiser, *Phys. Rev. C* **92**, 015801 (2015).
- [18] J. E. Lynn, I. Tews, J. Carlson, S. Gandolfi, A. Gezerlis, K. E. Schmidt, and A. Schwenk, *Phys. Rev. Lett.* **116**, 062501 (2016).
- [19] C. Drischler, K. Hebeler, and A. Schwenk, *Phys. Rev. C* **93**, 054314 (2016).
- [20] A. Ekström, G. Hagen, T. D. Morris, T. Papenbrock, and P. D. Schwartz, *Phys. Rev. C* **97**, 024332 (2018).
- [21] A. Carbone, A. Polls, and A. Rios, *Phys. Rev. C* **98**, 025804 (2018).
- [22] C. Drischler, K. Hebeler, and A. Schwenk, *Phys. Rev. Lett.* **122**, 042501 (2019).
- [23] A. Carbone and A. Schwenk, *Phys. Rev. C* **100**, 025805 (2019).
- [24] B.-N. Lu, N. Li, S. Elhatisari, D. Lee, J. E. Drut, T. A. Lähde, E. Epelbaum, and Ulf-G. Meißner, *Phys. Rev. Lett.* **125**, 192502 (2020).
- [25] C. Drischler, R. J. Furnstahl, J. A. Melendez, and D. R. Phillips, *Phys. Rev. Lett.* **125**, 202702 (2020).
- [26] J. Keller, C. Wellenhofer, K. Hebeler, and A. Schwenk, *Phys. Rev. C* **103**, 055806 (2021).
- [27] K. Hebeler, J. M. Lattimer, C. J. Pethick, and A. Schwenk, *Astrophys. J.* **773**, 11 (2013).
- [28] E. Annala, T. Gorda, A. Kurkela, and A. Vuorinen, *Phys. Rev. Lett.* **120**, 172703 (2018).
- [29] E. R. Most, L. R. Weih, L. Rezzolla, and J. Schaffner-Bielich, *Phys. Rev. Lett.* **120**, 261103 (2018).
- [30] I. Tews, J. Margueron, and S. Reddy, *Phys. Rev. C* **98**, 045804 (2018).
- [31] Y. Lim and J. W. Holt, *Phys. Rev. Lett.* **121**, 062701 (2018).
- [32] C. D. Capano, I. Tews, S. M. Brown, B. Margalit, S. De, S. Kumar, D. A. Brown, B. Krishnan, and S. Reddy, *Nat. Astron.* **4**, 625 (2020).
- [33] R. Essick, I. Tews, P. Landry, S. Reddy, and D. E. Holz, *Phys. Rev. C* **102**, 055803 (2020).
- [34] T. Dietrich, M. W. Coughlin, P. T. H. Pang, M. Bulla, J. Heinzel, L. Issa, I. Tews, and S. Antier, *Science* **370**, 1450 (2020).
- [35] G. Raaijmakers, S. K. Greif, K. Hebeler, T. Hinderer, S. Nisanke, A. Schwenk, T. E. Riley, A. L. Watts, J. M. Lattimer, and W. C. G. Ho, *Astrophys. J. Lett.* **918**, L29 (2021).
- [36] R. Essick, I. Tews, P. Landry, and A. Schwenk, *Phys. Rev. Lett.* **127**, 192701 (2021).
- [37] C. Drischler, S. Han, J. M. Lattimer, M. Prakash, S. Reddy, and T. Zhao, *Phys. Rev. C* **103**, 045808 (2021).
- [38] S. Huth, P. T. H. Pang, I. Tews, T. Dietrich, A. Le Fèvre, A. Schwenk, W. Trautmann, K. Agarwal, M. Bulla, M. W. Coughlin *et al.*, *Nature (London)* **606**, 276 (2022).
- [39] A. L. Fetter and J. D. Walecka, *Quantum Theory of Many-Particle Systems* (McGraw-Hill, New York, 1972).
- [40] J. W. Negele and H. Orland, *Quantum Many-Particle Systems* (Westview Press, Boulder, CO, 1998).
- [41] D. R. Entem, R. Machleidt, and Y. Nosyk, *Phys. Rev. C* **96**, 024004 (2017).
- [42] K. Hebeler, *Phys. Rep.* **890**, 1 (2021).
- [43] W. Kohn and J. M. Luttinger, *Phys. Rev.* **118**, 41 (1960).
- [44] C. Wellenhofer, *Phys. Rev. C* **99**, 065811 (2019).
- [45] C. E. Rasmussen and C. K. I. Williams, *Gaussian Processes for Machine Learning* (MIT Press, Cambridge, MA, 2005).
- [46] M. A. Chilenski, M. Greenwald, Y. Marzouk, N. T. Howard, A. E. White, J. E. Rice, and J. R. Walk, *Nucl. Fusion* **55**, 023012 (2015).
- [47] C. J. Horowitz and A. Schwenk, *Phys. Lett. B* **638**, 153 (2006).
- [48] C. J. Horowitz and A. Schwenk, *Nucl. Phys.* **A776**, 55 (2006).
- [49] E. Epelbaum, H. Krebs, and U.-G. Meißner, *Eur. Phys. J. A* **51**, 53 (2015).
- [50] J. M. Lattimer and F. D. Swesty, *Nucl. Phys.* **A535**, 331 (1991).
- [51] C. Drischler, J. A. Melendez, R. J. Furnstahl, and D. R. Phillips, *Phys. Rev. C* **102**, 054315 (2020).